

## On the three-dimensional Rayleigh–Taylor instability

Xiaoyi He, Raoyang Zhang, Shiyi Chen, and Gary D. Doolen

Citation: [Phys. Fluids](#) 11, 1143 (1999); doi: 10.1063/1.869984

View online: <http://dx.doi.org/10.1063/1.869984>

View Table of Contents: <http://pof.aip.org/resource/1/PHFLE6/v11/i5>

Published by the [American Institute of Physics](#).

---

### Additional information on Phys. Fluids

Journal Homepage: <http://pof.aip.org/>

Journal Information: [http://pof.aip.org/about/about\\_the\\_journal](http://pof.aip.org/about/about_the_journal)

Top downloads: [http://pof.aip.org/features/most\\_downloaded](http://pof.aip.org/features/most_downloaded)

Information for Authors: <http://pof.aip.org/authors>

### ADVERTISEMENT



**Running in Circles Looking  
for the Best Science Job?**

**Search hundreds of exciting  
new jobs each month!**

<http://careers.physicstoday.org/jobs>

**physicstodayJOBS**



# On the three-dimensional Rayleigh–Taylor instability

Xiaoyi He, Raoyang Zhang, Shiyi Chen, and Gary D. Doolen

*Los Alamos National Laboratory, Los Alamos, New Mexico 87545*

(Received 20 October 1998; accepted 13 January 1999)

The three-dimensional Rayleigh–Taylor instability is studied using a lattice Boltzmann scheme for multiphase flow in the nearly incompressible limit. This study focuses on the evolution of the three-dimensional structure of the interface. In addition to the bubble and spike fronts, a saddle point is found to be another important landmark on the interface. Two layers of heavy-fluid roll-ups, one at the spike tip and the other at the saddle point, were observed. The secondary instability in the horizontal planes entangles the already complicated structure of the interface. Parallel computations are utilized to accommodate the massive computational requirements of the simulations. © 1999 American Institute of Physics. [S1070-6631(99)00605-4]

## I. INTRODUCTION

The Rayleigh–Taylor instability occurs when an interface between two different fluids with different densities experiences a pressure gradient opposing the density gradient. This interface is unstable and any disturbance tends to grow, leading to the penetration of both fluids into each other. If the initial interface displacement is random, the Rayleigh–Taylor instability usually evolves into complicated turbulent mixing.

The Rayleigh–Taylor instability has attracted much attention because of its significance in both fundamental research and engineering applications. In fundamental research, the Rayleigh–Taylor instability provides an ideal system to study multiphase hydrodynamical instabilities, turbulent mixing, and supernovae dynamics. In engineering applications, the Rayleigh–Taylor instability plays a key role in inertial confinement fusion.

Much knowledge concerning the Rayleigh–Taylor instability has been gained in the past 50 years. Following Sharp,<sup>1</sup> we can roughly divide the growth of the instability into four stages. In the first stage, the amplitude of the surface perturbation is much smaller than its wavelength and the amplitude grows exponentially with time.<sup>2</sup> The Rayleigh–Taylor instability in this stage can be studied using linear stability theory and the linear growth rate has been found as a function of the density ratio, the viscosities, the surface tension, and the compressibility.<sup>2–4</sup> Linear perturbation theory fails when the amplitude of the perturbation grows to 10%–40% of its wavelength. This failure of linear perturbation theory marks the beginning of the second stage of the Rayleigh–Taylor instability. During the second stage, the perturbation grows nonlinearly to form bubbles of light fluid rising into the heavy fluid and spikes of heavy fluid falling into the light fluid. This stage of development is strongly influenced by three-dimensional effects and the density ratio. Experiments<sup>5,6</sup> and numerical simulations<sup>7–9</sup> have shown that the bubbles rise at an approximately constant velocity during this stage.

The third stage of Rayleigh–Taylor instability is characterized by the development of additional structures on the

spikes and by interactions among the bubbles. The Kelvin–Helmholtz instability begins to develop at this time and the heavy fluid begins to roll up along the sides of the spikes to form “mushrooms.” This phenomenon is more pronounced when the density ratio is low. The interaction among bubbles is likely due to the interaction among initial perturbations of different wavelengths. Eventually, this interaction evolves into turbulent or chaotic mixing which dominates the fourth stage of the Rayleigh–Taylor instability. Little is known about this turbulent-mixing stage, although a number of experiments<sup>6</sup> and numerical simulations<sup>10,11</sup> suggest that the thickness of the mixing layer increases quadratically with time.

The above discussion only gives a qualitative description of the Rayleigh–Taylor instability. Except for the initial linear growth stage, quantitative knowledge is limited especially in three dimensions. To the best of our knowledge, there have been only a few numerical studies of the three-dimensional Rayleigh–Taylor instability<sup>9,12–16</sup> and simulations of the late stage instability are quite rare. How the three-dimensional interface evolves in the nonlinear growth stages has not been well documented. The research goal of the current study is to help to fill this gap. For simplicity, we choose to study the single-mode three-dimensional Rayleigh–Taylor instability. Special attention is paid to the evolution of the interface and to the role of three-dimensional effects at late stages. The important role of the secondary instability in horizontal planes will also be discussed.

In this study, direct numerical simulations of three-dimensional Rayleigh–Taylor instability were carried out using the lattice Boltzmann method (LBM). The lattice Boltzmann method has emerged as a useful approach of computational fluid dynamics (CFD). (For a review, see Ref. 17.) Unlike traditional CFD methods which solve the macroscopic governing equations, the lattice Boltzmann method simulates multiphase flow based on a mesoscopic kinetic equation. The interfacial dynamics, which are important in multiphase flow and are difficult to handle in traditional methods, can be easily modeled in the LBM by incorporating

molecular interactions.<sup>18–21</sup> Recently, we proposed a new robust lattice Boltzmann method for simulations of incompressible multiphase flow.<sup>22</sup> Benchmark studies using this method yield satisfactory results for the two-dimensional Rayleigh–Taylor instability. In this study, this method is further extended to simulate the three-dimensional Rayleigh–Taylor instability. Parallel computations are utilized to accommodate the massive computational requirements.

The rest of the paper is organized as follows: In Sec. II, we give a brief description of the lattice Boltzmann method for incompressible multiphase flow. Issues related to the parallelization of the computer code will also be addressed in this section. Section III presents numerical results of the three-dimensional Rayleigh–Taylor instability. A brief conclusion is given in Sec. IV.

## II. METHODOLOGY

### A. Lattice Boltzmann method for incompressible multiphase flow

The lattice Boltzmann method simulates fluid flows based on discrete distribution functions.<sup>17</sup> For multiphase flows in the nearly incompressible limit, the fluid density of each component is assumed to be constant. In this scenario, it is useful to introduce an index function to track the interfaces between the two different phases and to replace the density distribution function with a pressure distribution function. The distribution functions satisfy the following evolution equations:<sup>22</sup>

$$\begin{aligned} \bar{f}_\alpha(\mathbf{x} + \mathbf{e}_\alpha \delta_t, t + \delta_t) - \bar{f}_\alpha(\mathbf{x}, t) \\ = - \frac{\bar{f}_\alpha(\mathbf{x}, t) - f_\alpha^{\text{eq}}(\mathbf{x}, t)}{\tau} \\ + \frac{(2\tau - 1)}{2\tau} \frac{(\mathbf{e}_\alpha - \mathbf{u}) \cdot \nabla \psi(\phi)}{RT} \Gamma_\alpha(\mathbf{u}) \delta_t, \end{aligned} \quad (1)$$

$$\begin{aligned} \bar{g}_\alpha(\mathbf{x} + \mathbf{e}_\alpha \delta_t, t + \delta_t) - \bar{g}_\alpha(\mathbf{x}, t) \\ = - \frac{\bar{g}_\alpha(\mathbf{x}, t) - g_\alpha^{\text{eq}}(\mathbf{x}, t)}{\tau} + \frac{2\tau - 1}{2\tau} (\mathbf{e}_\alpha - \mathbf{u}) \cdot [\Gamma_\alpha(\mathbf{u}) \\ \times (\mathbf{F}_s + \mathbf{G}) - (\Gamma_\alpha(\mathbf{u}) - \Gamma_\alpha(0)) \nabla(p - \rho RT)] \delta_t, \end{aligned} \quad (2)$$

where  $\bar{f}_\alpha$  and  $\bar{g}_\alpha$  are related to the distribution functions of the index function and pressure,  $f_\alpha$  and  $g_\alpha$ , by:

$$\bar{f}_\alpha = f_\alpha - \frac{(\mathbf{e}_\alpha - \mathbf{u}) \cdot \nabla \psi(\phi)}{2RT} \Gamma_\alpha(\mathbf{u}) \delta_t, \quad (3)$$

$$\begin{aligned} \bar{g}_\alpha = g_\alpha - \frac{1}{2} (\mathbf{e}_\alpha - \mathbf{u}) \cdot [\Gamma_\alpha(\mathbf{u}) (\mathbf{F}_s + \mathbf{G}) - (\Gamma_\alpha(\mathbf{u}) \\ - \Gamma_\alpha(0)) \nabla(p - \rho RT)] \delta_t, \end{aligned} \quad (4)$$

and

$$\Gamma_\alpha(\mathbf{u}) = w_\alpha \left[ 1 + \frac{\mathbf{e}_\alpha \cdot \mathbf{u}}{RT} + \frac{(\mathbf{e}_\alpha \cdot \mathbf{u})^2}{2(RT)^2} - \frac{\mathbf{u}^2}{2RT} \right]. \quad (5)$$

As shown in Ref. 21, the introduction of  $\bar{f}_\alpha$  and  $\bar{g}_\alpha$  preserves the scheme's second-order accuracy in time, which is necessary for a correct multiphase LBM model.  $f_\alpha^{\text{eq}}$  and  $g_\alpha^{\text{eq}}$  are the corresponding equilibrium distributions:

$$f_\alpha^{\text{eq}} = w_\alpha \phi \left[ 1 + \frac{\mathbf{e}_\alpha \cdot \mathbf{u}}{RT} + \frac{(\mathbf{e}_\alpha \cdot \mathbf{u})^2}{2(RT)^2} - \frac{\mathbf{u}^2}{2RT} \right], \quad (6)$$

$$g_\alpha^{\text{eq}} = w_\alpha \left[ p + \rho RT \left( \frac{\mathbf{e}_\alpha \cdot \mathbf{u}}{RT} + \frac{(\mathbf{e}_\alpha \cdot \mathbf{u})^2}{2(RT)^2} - \frac{\mathbf{u}^2}{2RT} \right) \right], \quad (7)$$

where  $R$  is the gas constant,  $T$  is the background temperature, and  $w_\alpha$  are integral weights which depends on the discrete velocities used.

In the above evolution equations, we have used the single-relaxation-time BGK model.<sup>23</sup> The relaxation time is  $\tau \delta_t$  which in turn is related to the kinematic viscosity by  $\nu = (\tau - \frac{1}{2})$ , where  $\delta_t$  is the time step usually taken as the time unit in the LBM. The other parameters are the gravity force,  $\mathbf{G}$ , and the surface-tension-related force:

$$\mathbf{F}_s = \kappa \rho \nabla \nabla^2 \rho, \quad (8)$$

where  $\kappa$  determines the magnitude of the surface tension.

The distribution functions can be used to calculate the index function  $\phi$ , the pressure  $p$ , and the macroscopic velocity  $\mathbf{u}$ :

$$\phi = \sum \bar{f}_\alpha, \quad (9)$$

$$p = \sum \bar{g}_\alpha - \frac{1}{2} \mathbf{u} \cdot \nabla(p - \rho RT) \delta_t, \quad (10)$$

$$\rho RT \mathbf{u} = \sum \mathbf{e}_\alpha \bar{g}_\alpha + \frac{RT}{2} (\mathbf{F}_s + \mathbf{G}) \delta_t. \quad (11)$$

The density and the kinematic viscosity can be calculated from the index function using:

$$\rho(\phi) = \rho_l + \frac{\phi - \phi_l}{\phi_h - \phi_l} (\rho_h - \rho_l), \quad (12)$$

$$\nu(\phi) = \nu_l + \frac{\phi - \phi_l}{\phi_h - \phi_l} (\nu_h - \nu_l), \quad (13)$$

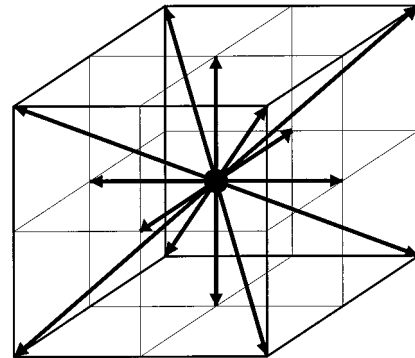


FIG. 1. The 15-speed lattice model of the three-dimensional lattice Boltzmann method.

where  $\rho_l$  and  $\rho_h$  are densities of light fluid and heavy fluid, respectively;  $\nu_l$  and  $\nu_h$  are viscosities of the light fluid and the heavy fluid, respectively;  $\phi_l$  and  $\phi_h$  are the minimum and maximum values of the index function.

In the above evolution equations,  $\mathbf{e}_a$  is a set of discrete microscopic velocities along which we track the discrete distribution functions. The choice of the discrete velocities is

$$[\mathbf{e}_0, \mathbf{e}_1, \dots, \mathbf{e}_{14}] = \begin{bmatrix} 0 & c & -c & 0 & 0 & 0 & 0 & c & -c & c & -c & c & -c & c & -c \\ 0 & 0 & 0 & c & -c & 0 & 0 & c & -c & c & -c & -c & c & -c & c \\ 0 & 0 & 0 & 0 & 0 & c & -c & c & -c & -c & c & -c & c & c & -c \end{bmatrix}, \quad (14)$$

where  $c = \sqrt{3RT}$  is the lattice speed. The corresponding integral weights in Eqs. 6 and 7 are:

$$[w_0, w_1, \dots, w_{14}] = \left[ \frac{2}{9}, \frac{1}{9}, \frac{1}{9}, \frac{1}{9}, \frac{1}{9}, \frac{1}{9}, \frac{1}{9}, \frac{1}{9}, \frac{1}{72}, \frac{1}{72}, \frac{1}{72}, \frac{1}{72}, \frac{1}{72}, \frac{1}{72}, \frac{1}{72} \right]. \quad (15)$$

Using the Chapman–Enskog expansion, we can prove that the above evolution equations recover the macroscopic Navier–Stokes equations for multiphase flow.<sup>27,28</sup>

The function  $\psi(\phi)$  in Eq. (1) plays a key role in multiphase flow simulations. The term  $\nabla\psi(\phi)$  is a mimic of the physical intermolecular interactions in nonideal gases or dense fluids. Unlike those in an ideal gas, molecules in dense fluids experience interactions with neighboring molecules.<sup>29</sup> Collisions among molecules in dense fluids are also strongly affected by the density.<sup>30</sup> Using the mean-field approximation, these two effects can be incorporated into an effective force  $\nabla\psi(\rho)$  and a surface tension force  $\mathbf{F}_s$ .<sup>21</sup> The surface tension force exclusively contributes to the surface tension. The effective force,  $\nabla\psi(\rho)$ , on the other hand, determines the phase segregation.

In general,  $\psi$  can be written as the following form:<sup>21</sup>

$$\psi(\rho) = b\rho^2 RT\chi(\rho) - a\rho^2, \quad (16)$$

in which the first term is due to the effect of fluid density on the molecular collision rate and the second term is due to intermolecular attractions. Phase segregation occurs when the fluid temperature is reduced below a critical value or when the intermolecular attraction becomes larger than a critical value. There is usually one range of density in which  $dp/dV$  becomes positive—a mechanically unstable state. For any density in this range, phase separation occurs.

The same physical mechanism can be applied to the index function. As long as the function  $\psi(\phi)$  is appropriately chosen so that there exists an unstable range of  $\phi$  in which  $d(\psi + \phi RT)/d\phi < 0$ , the index function can only exist in two separate stable states. Interfaces between different phases remain sharp automatically. In this study, we adopt the following equation for  $\psi(\phi)$ :

$$\psi(\phi) = \phi^2 RT \frac{4 - 2\phi}{(1 - \phi)^3} - a\phi^2. \quad (17)$$

This relation can be derived from the Carnahan–Starling equation of state.<sup>31</sup> Figure 2 shows the coexistence curve of

not arbitrary. It is restricted by conservation laws and the requirement of lattice symmetry in order to obtain the correct hydrodynamics.<sup>24</sup> Mathematically, this requires that the discrete integration formula based on  $\mathbf{e}_a$  has to be accurate to a certain order.<sup>25</sup> In three dimensions, one of the lattice structures that satisfies these restrictions is the following 15-speed model shown in Fig. 1:<sup>26</sup>

$\phi$  based on Eq. (17). The critical value of  $a$  is  $a_c = 10.601RT$  above which  $\phi$  can only exist in two stable states. This study chooses  $a = 12RT$  or  $a_c/a = 0.883$ . The corresponding transition values for  $\phi$  are 0.040 and 0.259.

## B. Parallel computations

Numerical simulations of the three-dimensional Rayleigh–Taylor instability require massive computational resources. In this study, we take advantage of the recent developments in parallel computation techniques. The code used in this study is written in FORTRAN90 with Message Passing Interface (MPI). MPI is a paradigm used widely on certain classes of parallel machines, especially those with distributed memory. With this communication standard, computations can be distributed evenly across multiprocessors. Each processor does the calculation for a sub-domain and it exchanges information on the sub-domain boundary with other processors. By using this MPI algorithm, the computational speed and memory can increase almost linearly with the number of the processors used.

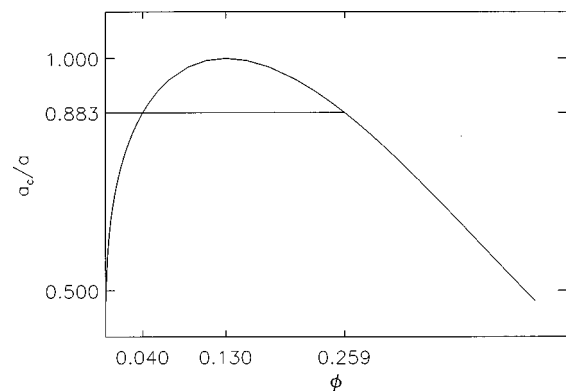


FIG. 2. Coexistence curve of  $\phi$ . The critical point is at  $\phi_c = 0.130$  and  $a_c = 10.601RT$ .

The lattice Boltzmann method is known for its efficiency in parallel computation. Since the explicit LBM scheme is purely local, the massive MPI communication, which is the most time consuming procedure in the parallel computation, is greatly reduced. The basic operations in the single-phase LBM are streaming and collision. An additional operation in our multiphase LBM scheme is the finite differencing required to calculate the forces ( $\nabla\phi$  and  $\rho\nabla\nabla^2\rho$ ). In our simulations, the computational domains are always sliced in one direction. Consequently, the streaming and finite differencing require only one layer of communication between neighboring processors. Therefore, the total communication is reduced compared with traditional schemes.

All simulations in this study are carried out on the ASCI BlueMountain machine—a parallel machine composed of SGI Origin 2000s at the Los Alamos National Lab. This parallel machine has a few hundred processors with 256 Megabytes of memory for each node. A typical simulation on a  $64\times 64\times 256$  grid takes less than 8 CPU hours using 16 nodes. For high resolution simulation on a  $128\times 128\times 512$  grid, more than 5 Gbytes of memory is required and the total computational time is about 80 hours using 32 nodes. Note the total number of time steps required for our high-resolution simulation is twice as large as the total number of time steps required for our low-resolution simulation.

### III. RESULTS

We simulated the three-dimensional Rayleigh–Taylor instability in a rectangular box with a square horizontal cross section. The height–width aspect ratio was fixed at 4:1. The gravity pointed downward and surface tension was neglected. For simplicity, the kinematic viscosities were chosen to be the same for both heavy and light fluids. Periodic boundary conditions were applied at the four sides, while nonslip boundary conditions were applied at the top and bottom walls. The instability develops from the imposed single-mode initial perturbation:

$$\frac{h(x,y)}{W} = 0.05 \left[ \cos\left(\frac{2\pi x}{W}\right) + \cos\left(\frac{2\pi y}{W}\right) \right], \quad (18)$$

where  $h$  is the height of the interface and  $W$  is the box width. Unless otherwise specified, the origin of the coordinates is at the lower left bottom corner of the box.

The results are presented in dimensionless quantities. The box width,  $W$ , is taken as the length scale and  $T = \sqrt{W/g}$  is taken as the time scale, where  $g$  is the gravitational acceleration. The dimensionless parameters in this study are the Reynolds number,  $Re = \sqrt{Wg}W/\nu$  where  $\nu$  is the kinematic viscosity, and the Atwood number,  $A = (\rho_h - \rho_l)/(\rho_h + \rho_l)$  where  $\rho_h$  and  $\rho_l$  are densities of heavy and light fluids, respectively.

The typical evolution of the fluid interface in the three-dimensional Rayleigh–Taylor instability is shown in Fig. 3. The Atwood and Reynolds numbers are 0.5 and 1024, respectively. The simulation is carried out on a  $128\times 128\times 512$  grid. Presented in the figure are views of the interface from both the heavy-fluid side (left panel) and the light-fluid side (right panel). As expected, the heavy and light fluids pen-

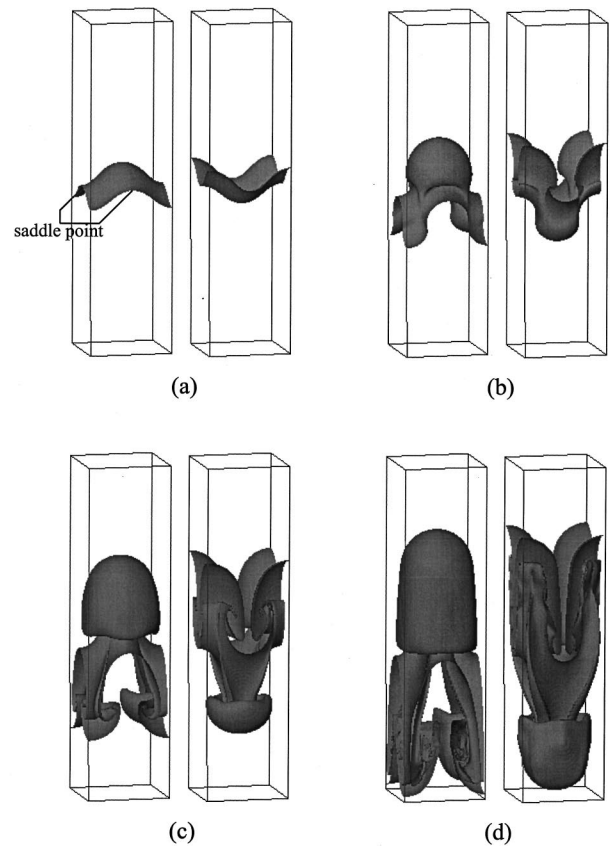


FIG. 3. Evolution of the fluid interface from a single-mode perturbation at (a)  $t=1.0$ , (b)  $t=2.0$ , (c)  $t=3.0$ , and (d)  $t=4.0$ . The Atwood number is 0.5 and the Reynolds number is 1024. Time is measured in units of  $\sqrt{W/g}$ . The interface is viewed from the heavy-fluid side (left panel) and from the light-fluid side (right panel). The interfaces in the left panel are shifted  $W/2$  in both  $x$  and  $y$  directions for a better view of the bubble.

etrate into each other as time increases. The light fluid rises to form a bubble and the heavy fluid falls to generate a spike. Furthermore, there is an additional landmark that distinguishes this interface from that observed in a two-dimensional Rayleigh–Taylor instability; that is, the existence of four saddle points at the middle of the four sides of the computational box shown in Fig. 3(a). The evolution of the interface around these saddle points is one of the unique features of the three-dimensional Rayleigh–Taylor instability.

As shown in Fig. 3, the interface remains rather simple during the early stage [Fig. 3(a)] but becomes more complicated as time increases. For this typical case, the Kelvin–Helmholtz instability does not develop until  $t=2.0$  when the first roll-up of the heavy fluid appears in the neighborhood of the saddle points [Fig. 3(b)]. The roll-up at the edge of the spike starts at a later time [Fig. 3(c)]. At  $t=4.0$ , these roll-ups have been stretched into two extra layers of heavy fluid folded upward: one forms a skirt around the spike and the other forms a girdle inside the bubble [Fig. 3(d)]. Notice also the small curls inside the skirt. These structures are formed by the Kelvin–Helmholtz instability. From the outside, both the bubble and spike look like mushrooms. A similar evolution of the interface was observed in other numerical

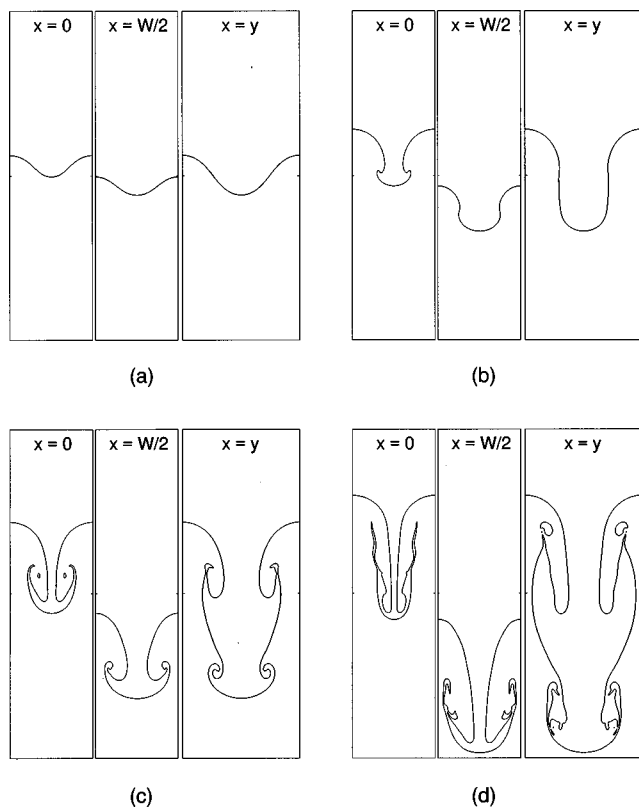


FIG. 4. Cross-sectional views of the interface at three vertical planes,  $x=0$ ,  $x=W/2$ , and  $x=y$ ; (a)  $t=1.0$ , (b)  $t=2.0$ , (c)  $t=3.0$ , and (d)  $t=4.0$ . The Atwood number is 0.5 and the Reynolds number is 1024.

simulations<sup>12,14</sup> although they were not carried out to this late stage. This two-layer roll-up phenomenon is another unique feature of the three-dimensional Rayleigh–Taylor instability.

To track more closely the interface evolution, we plotted in Fig. 4 the interface in three vertical planes:  $x=0$ ,  $x=W/2$ , and  $x=y$ . The interfaces in the  $x=0$  and  $x=W/2$  planes look very much like those in the two-dimensional Rayleigh–Taylor instability.<sup>8,10,22</sup> The heavy-fluid stem and roll-up in the  $x=0$  plane are smaller than those in the  $x=W/2$  plane. However, the interface in the  $x=y$  plane is quite different. The two-layer roll-up phenomenon can be clearly seen in this plane. A similar result was also observed in a recent study using the untracked finite difference method for solving Euler’s equation.<sup>14</sup> These two-layer roll-ups should not be confused with the multiple roll-ups observed in the two-dimensional Rayleigh–Taylor instability. The former should be attributed to the instabilities at two different locations, namely the spike tip and the saddle point; while the latter is due to the Kelvin–Helmholtz instability in the same shear layers.

Figure 5 shows the time evolutions of the bubble front, the spike tip, and the saddle point. The growth of the bubble and spike in the early stage are consistent with the theoretically predicted exponential growth. At later times, the bubble tends to rise at a constant speed. The terminal velocity of the bubble, in units of  $\sqrt{AgW/2}$ , was measured at 0.61 for  $A=0.5$ . This value is comparable to the results of 0.56 for  $A=0.67$  and 0.63 for  $A=0.33$  reported in a previous study using the untracked finite difference method for solving Eu-

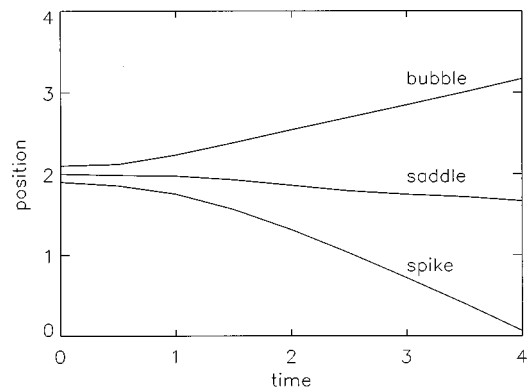


FIG. 5. Positions of the bubble front, spike tip, and saddle point versus time. The Atwood number is 0.5 and the Reynolds number is 1024. The length is measured in units of  $W$  and time is measured in units of  $\sqrt{W/g}$ .

ler’s equation.<sup>9</sup> It is also close to the value of 0.57 reported by Abarzhi<sup>32</sup> and 0.62 by Glimm *et al.*<sup>16</sup> The spike settles into a constant-speed state at intermediate times, but tends to accelerate slightly at later times. The saddle points move downward as time increases, but the movement is rather slow at this Atwood number. Both the bubble and spike move faster in three dimensions than they do in two-dimensions. This is consistent with the observations of Yabe *et al.*<sup>13</sup>

The complicated structures of the interface at the late stage can be seen clearly in horizontal cross sections. As an example, we show the results at  $t=4.0$  from the same simulation [see Fig. 3(d)]. We found it is helpful to present the interfaces above the saddle points separately from those below the saddle points. Figure 6 shows the density plots at a number of horizontal planes above the saddle point. The plane is labeled by the grid index  $k \in [1, 512]$  and the plane altitude can be found using  $z=k/128$ . At the saddle point level ( $k=213$ ), the light fluid exhibits the shape of a “rosette” with the petals pointing towards the saddle points. Moving upward, the “rosette” quickly contracts its petals and becomes embedded in a box of heavy fluid ( $k=220$ ). At a slightly higher level ( $k=230$ ), the surrounding heavy fluid is divided into two parts by a ring of light fluid. This ring of light fluid comes from the outer layer of the mushroom of the bubble; while the heavy fluid between the “rosette” and the light fluid ring comes from the roll-up girdle of the heavy fluid around the saddle points. A similar structure persists all the way up to  $k=300$ . Above that level, the “rosette” of light fluid in the middle gradually transforms into a “diamond” shape ( $k=320-360$ ). In the meantime, the girdle of the heavy fluid shrinks and finally disappears at  $k=370$ . Above  $k=370$ , only a bubble of light fluid is visible.

Figure 7 shows the density plots for a number of horizontal planes below the saddle points. Across the bottom of the spike, the blob of the heavy fluid has a roughly rectangular shape at  $k=20$ . At slightly higher levels ( $k=30-40$ ), this simple geometry is replaced by a configuration with a core of heavy fluid in the middle surrounded by a frame of heavy fluid. The heavy-fluid core forms a cross with its bars oriented diagonally. The frame is a skirt of heavy fluid which has rolled up around the spike. Between the heavy-fluid core

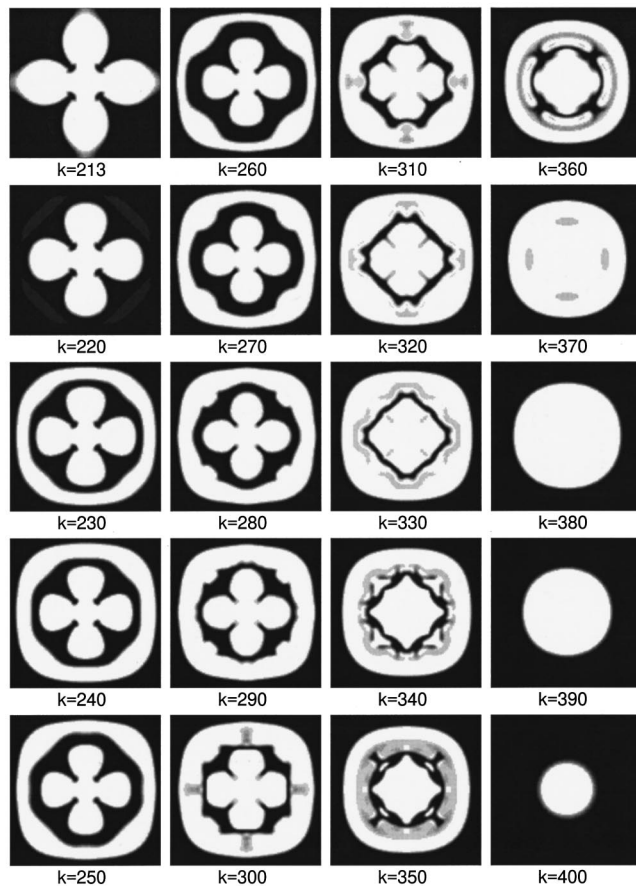


FIG. 6. Density plots at  $t=4.0$  in horizontal planes above the saddle points. Black represents the heavy fluid and white represents the light fluid. The plots are shifted  $W/2$  in both  $x$  and  $y$  directions for a better view of the bubble. The Atwood number is 0.5 and the Reynolds number is 1024. The plane altitude can be calculated using  $z = k/128$ .

and the frame is a gap of light fluid. Moving upward, the heavy-fluid frame gradually transforms from its original square shape to a roughly circular shape until it finally disappears near  $k=120$ . For  $k$  between 70 and 110, we can see another layer of heavy fluid which represents the folding back of the heavy-fluid skirt. The wavy interface indicates that an instability may start to develop in these horizontal planes.

Regarding the instability in horizontal planes, it is interesting to notice what happens at the tips of the cross of the heavy-fluid core. Starting from  $k=60$ , the tips of the cross begin to widen and the heavy fluid begins to roll inward. At  $k=90$ , these tips have transformed into an “anchor” shape. The same configuration persists all the way up to the saddle level, although the roll-ups begin to shrink at  $k=170$ . This roll-up phenomenon in the horizontal planes is very similar to that observed in the exploding Richtmyer–Meshkov instability.<sup>33</sup> However, they are not exactly the same because in our study we do not have an explicit outward force.

The formation of the various interface patterns in the horizontal planes is a direct consequence of the complicated velocity fields in the three-dimensional Rayleigh–Taylor instability. Figure 8 shows a few typical flow patterns in cer-

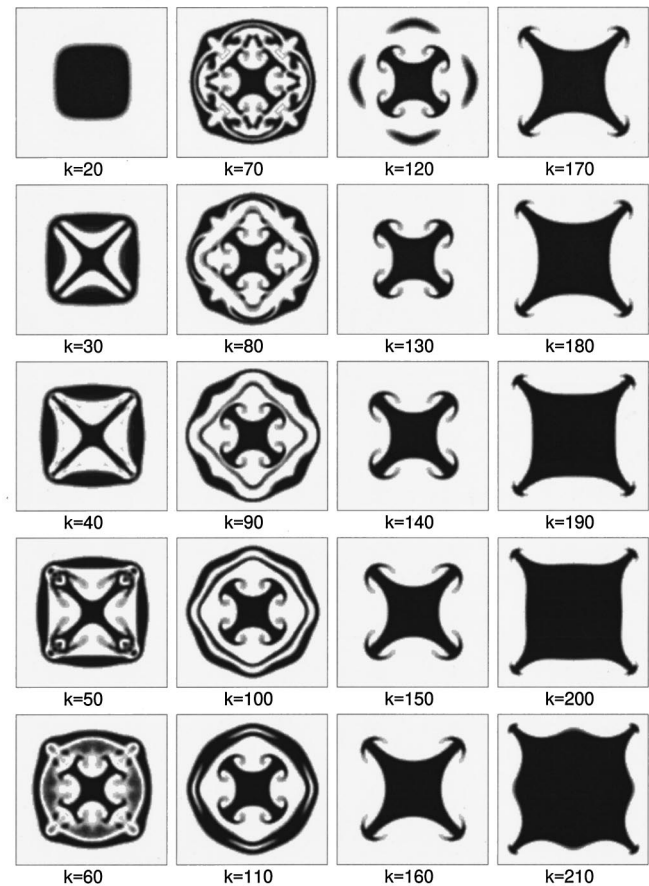


FIG. 7. Density plots at  $t=4.0$  in horizontal planes below the saddle points. Black represents the heavy fluid and white represents the light fluid. The Atwood number is 0.5 and the Reynolds number is 1024. The plane altitude can be calculated using  $z = k/128$ .

tain horizontal planes. Near the bubble front ( $k=380$ ), the light fluid pushes the heavy fluid outward and the velocity field is relatively symmetric with respect to the bubble center. In the middle layer of the bubble ( $k=320$ ), the secondary flow is weak but one can still see four pairs of counter-rotating vortices. Around the saddle point at  $k=220$ , the heavy fluid squeezes the light fluid radially inward. The velocity is not isotropic and the highest speed occurs along the diagonals. Near the spike tip ( $k=20$ ), the heavy fluid pushes the light fluid outward and the highest velocity occurs near the interface. The most complicated flow pattern occurs in the middle layer of the spike skirt ( $k=80$ ), where two layers of vortices are visible. Each vortex layer has four pairs of counter-rotating vortices. The counter-rotating pairs of vortices are also evident at  $k=150$ . Obviously, the mushroom at the tip of the heavy-fluid core is created by the vortices in the horizontal planes.

Another interesting feature of the Rayleigh–Taylor instability is the growth of the mixing layer. This can be quantified by the density averaged over the horizontal planes. Although this quantity has only been used for the multiple-mode Rayleigh–Taylor instability,<sup>10,34</sup> it also helps to understand the complicated structure of the single-mode Rayleigh–Taylor instability. Figure 9 displays the averaged



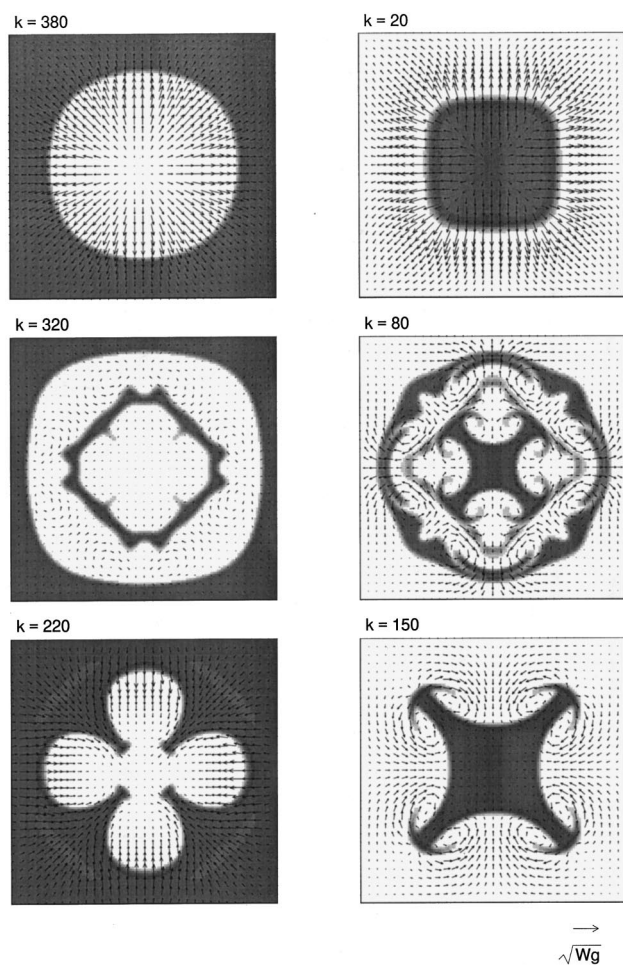


FIG. 8. Velocity vector plots in a number of horizontal planes at  $t=4.0$ . In the left panel are plots at levels above the saddle points. In the right panel are plots at levels below the saddle point. The arrow shows the characteristic velocity,  $\sqrt{Wg}$ . The Atwood number is 0.5 and the Reynolds number is 1024. The gray color indicates the heavy fluid.

density versus the height for four different time steps in the above simulation. To help understanding, we also marked the positions of the spike tip ( $\diamond$ ), the bubble front ( $\triangle$ ), and the saddle points ( $\square$ ). As expected, the mixing zone spreads out as time increases. However, unlike a pure diffusion process, the average density in the mixing zone peaks at certain positions after the initial stage. These peaks are due to the roll-ups of the heavy fluids and their movements naturally follow those of the spike tip or the saddle points. The first peak appears at  $t=2.0$  behind the saddle point. The peak behind the spike tip appears at a later time ( $t=3.0$ ). This result is consistent with the two-layer roll-up phenomenon observed in the previous figures. In addition to the two primary peaks mentioned above, a number of small peaks emerge at late stages. These small peaks correspond to the backward foldings of the roll-up tails. It is interesting to note that the evolution of the density profile above the saddle point is different from that below the saddle point. Above the saddle point, the primary peak persists and leaves a valley behind. Below the saddle point, the primary peak dwindles and coalesces with other small peaks to form a plateau ( $t=4.0$ ).

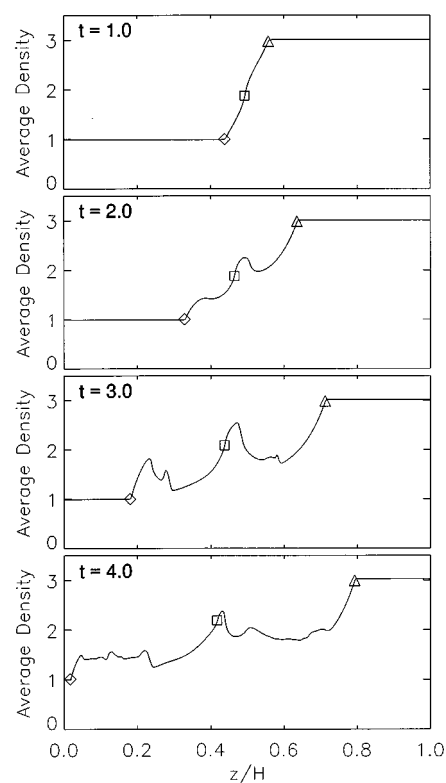


FIG. 9. Density averaged over horizontal planes versus height at four time steps.  $H$  is the height of the box. Also marked in the plots are the positions of the spike tip ( $\diamond$ ), the bubble front ( $\triangle$ ), and the saddle points ( $\square$ ). The Atwood number is 0.5 and the Reynolds number is 1024.

To study the effect of the viscosity on the three-dimensional Rayleigh–Taylor instability, we carried out numerical simulations at a number of Reynolds numbers with the Atwood number fixed at 0.5. Figure 10 shows the time dependencies of the bubble front, spike tip, and saddle point at different Reynolds numbers. As shown, an increase in viscosity or a decrease in Reynolds number retards the development of the Rayleigh–Taylor instability. This retardation is larger for the spike than for the bubble and saddle points.

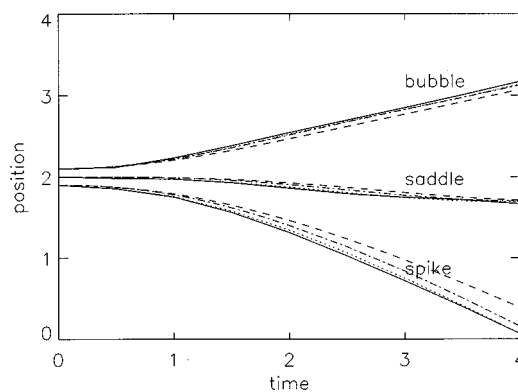


FIG. 10. Reynolds number dependence of the positions of the bubble front, spike tip, and saddle point. The Atwood number is fixed at 0.5. Solid line— $Re=1024$ ; dotted line— $Re=512$ ; dash-dotted line— $Re=256$ ; and dashed line— $Re=128$ . Length is measured in units of  $W$  and the time is measured in units of  $\sqrt{W/g}$ .



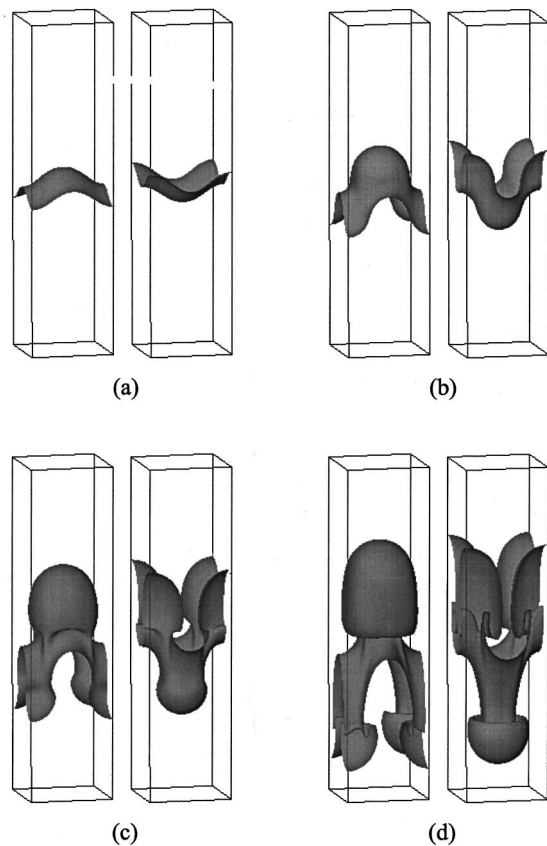


FIG. 11. Evolution of the fluid interface from a single-mode perturbation at (a)  $t=1.0$ , (b)  $t=2.0$ , (c)  $t=3.0$ , and (d)  $t=4.0$ . The Atwood number is 0.5 and the Reynolds number is 128. The interface is viewed from the heavy-fluid side (left panel) and from the light-fluid side (right panel).

The Reynolds-number dependence is noticeable at low Reynolds numbers but becomes negligible for  $Re > 512$ .

To illustrate the Reynolds-number dependence of interface structures, we plotted in Fig. 11 the evolution of the interface for  $Re=128$  and  $A=0.5$ . The simulation was carried out on a  $64 \times 64 \times 256$  grid. Compared with those in Fig. 3, the roll-ups or mushrooms appear at later times and they are substantially smaller. The complicated small structures along the roll-up skirt and girdle become smoothed out at this lower Reynolds number. This fact can also be confirmed by the cross-sectional plots of the interfaces in Fig. 12. In the  $x$  and  $y$  planes, the tails of the heavy-fluid roll-up are much shorter than those at the Reynolds number of 1024. In the diagonal plane ( $x=y$ ), the spike size is significantly reduced [Fig. 12(d)].

The three-dimensional Rayleigh–Taylor instability has a strong dependence on the density ratio. Figure 13 shows the interface evolution for an Atwood number of 0.9 and a Reynolds number of 128. The simulation was carried out on a  $64 \times 64 \times 256$  grid. Compared with that at  $A=0.5$ , the Rayleigh–Taylor instability at high Atwood number exhibits two different characteristics. First, the interface only possesses a small roll-up even at late stages, indicating that the Kelvin–Helmholtz instability plays a minor role at this high Atwood number. Second, the saddle points fall much faster than those at lower Atwood numbers (compared with Fig.

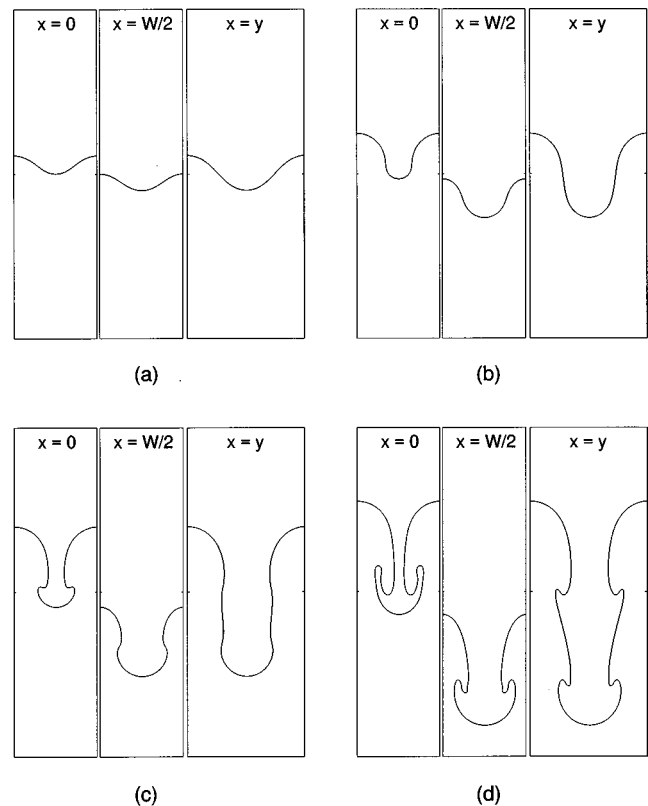


FIG. 12. Cross-sectional views of the interface at three vertical planes,  $x=0$ ,  $x=W/2$ , and  $x=y$ . (a)  $t=1.0$ , (b)  $t=2.0$ , (c)  $t=3.0$ , and (d)  $t=4.0$ . The Atwood number is 0.5 and the Reynolds number is 128.

11.) This more rapid fall of the saddle points has not been noted in other studies of three-dimensional Rayleigh–Taylor instability. It may depend on the specific initial condition adopted in this study.

The trajectories of the bubble front, spike tip, and saddle points at  $A=0.9$  are further quantified in Fig. 14. At this Atwood number, the bubble still tends to rise at a constant speed at late stages but the spike and saddle points appear to be in a free fall. The terminal bubble velocity, in units of  $\sqrt{AgW/2}$ , is 0.60 which is very close to the value of 0.61 for  $A=0.5$ . The accelerations of the spike and saddle points, in units of  $\sqrt{Ag}$ , are 0.7 and 0.6, respectively.

The Atwood number also influences the averaged density profile in the mixing layer. As shown in Fig. 15, the averaged density profile at  $A=0.9$  is much smoother than that at  $A=0.5$  (see Fig. 9 for a comparison). This result is consistent with the observation that the interface has fewer roll-ups at the higher Atwood number. The density peaks in the mixing zone still form first around the saddle point and then around the spike tip. Their appearances, however, were significantly delayed in time. Unlike that at low Atwood number, most of the density decrease in the density profile occurs near the bubble front.

Our simulation results appear to have satisfied grid convergence. As an example, Fig. 16 compares the interfaces in horizontal planes obtained on a  $64 \times 64 \times 256$  and a  $128 \times 128 \times 512$  grids. Except some local fine structures, the overall interface shape changes little with the grid refinement. More convergence studies can be found in Ref. 22.

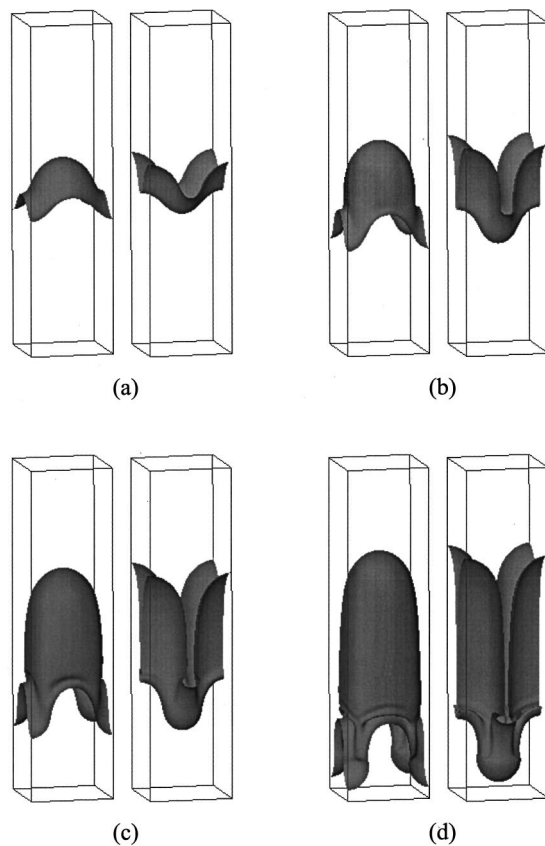


FIG. 13. Evolution of the fluid interface from a single mode perturbation at (a)  $t = 1.0$ , (b)  $t = 1.5$ , (c)  $t = 2.0$ , and (d)  $t = 2.5$ . The Atwood number is 0.9 and the Reynolds number is 128. The interface is viewed from the heavy-fluid side (left panel) and from the light-fluid side (right panel).

#### IV. CONCLUSIONS

The three-dimensional single-mode Rayleigh–Taylor instability was studied using a lattice Boltzmann scheme for incompressible multiphase flow. The study examined in detail the three-dimensional structure of the interface. In addition to the bubble and spike fronts, we found that the saddle point is another important landmark. Due to the Kelvin–Helmholtz instability, the heavy fluid tends to roll up at both the saddle point and the spike tip in the nonlinear growth

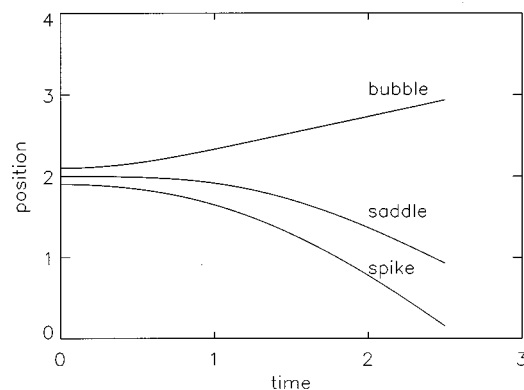


FIG. 14. Positions of the bubble front, spike tip, and saddle point versus time. The Atwood number is 0.9 and the Reynolds number is 128. The length is measured in units of  $W$  and time is measured in units of  $\sqrt{W/g}$ .

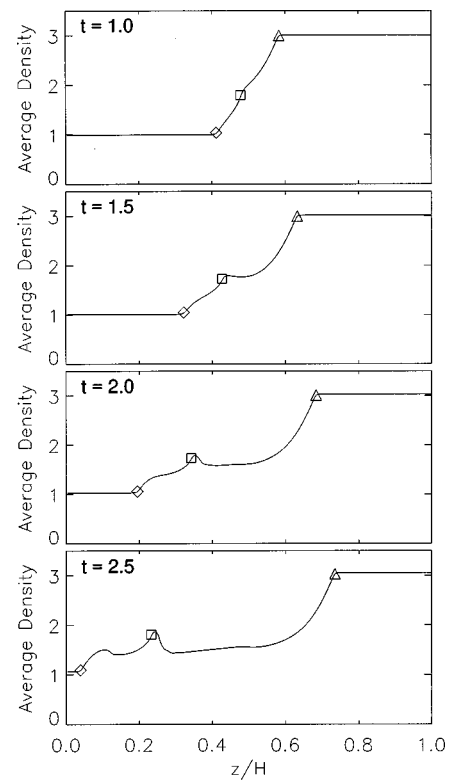


FIG. 15. Density averaged over horizontal planes versus height at four time steps.  $H$  is the height of the box. Also marked in the plots are the positions of the spike tip ( $\diamond$ ), the bubble front ( $\triangle$ ), and the saddle points ( $\square$ ). The Atwood number is 0.9 and the Reynolds number is 128.

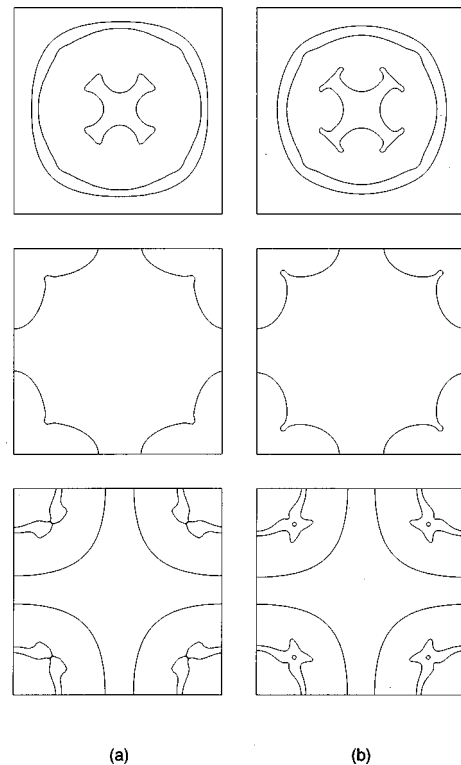


FIG. 16. Comparison of interfaces obtained on: (a) the  $64 \times 64 \times 256$  grid and (b) the  $128 \times 128 \times 512$  grid.

stage. Consequently, in the three-dimensional single-mode Rayleigh–Taylor instability, there are two layers of roll-up of the heavy fluid and this does not occur in the two-dimensional case.

In addition to being unstable in the vertical plane, the interface in the three-dimensional Rayleigh–Taylor instability is also observed to be unstable in the horizontal plane. This secondary instability is particularly prominent along the edge of the spike. For the typical initial perturbation used in this study, the interface in a horizontal plane across the spike tends to shrink in the  $x$  and  $y$  directions and protrude in the diagonal directions. The protrusion tips roll inward to form mushroom shapes in the horizontal planes. The secondary instability appears to be related strongly to the secondary flows in the horizontal planes. Counter-rotating vortices are always observed at the roll-up sites.

The trajectories of the bubble front, spike tip, and saddle point were quantified in this study. After an initial growth stage, the bubble front tends to rise at a constant velocity. The terminal bubble velocity, in units of  $\sqrt{AgW/2}$ , is approximately 0.60–0.61 and shows little dependence on the Atwood number. The spike at late stages moves at a relatively constant speed at a low Atwood number but undergoes a freefall at higher Atwood numbers. The movement of the saddle point is similar to that of spike.

## ACKNOWLEDGMENTS

This research is supported by the Department of Energy under Contract No. W-7405-ENG-36.

- <sup>1</sup>D. H. Sharp, "An overview of Rayleigh–Taylor instability," *Physica D* **12**, 3 (1984).
- <sup>2</sup>G. I. Taylor, "The instability of liquid surfaces when accelerated in a direction perpendicular to their planes. I," *Proc. R. Soc. London, Ser. A* **201**, 192 (1950).
- <sup>3</sup>S. Chandrasekhar, "The character of the equilibrium of an incompressible heavy viscous fluid of variable density," *Proc. Cambridge Philos. Soc.* **51**, 162 (1955).
- <sup>4</sup>M. Mitchner and R. K. M. Landshoff, "Rayleigh–Taylor instability for compressible fluids," *Phys. Fluids* **7**, 862 (1964).
- <sup>5</sup>R. M. Davies and G. I. Taylor, "The mechanics of large bubbles rising through extended liquids and through liquids in tubes," *Proc. R. Soc. London, Ser. A* **200**, 375 (1950).
- <sup>6</sup>K. I. Read, "Experimental investigation of turbulent mixing by Rayleigh–Taylor instability," *Physica D* **12**, 45 (1984).
- <sup>7</sup>J. Glimm, O. McBryan, R. Menikoff, and D. H. Sharp, "Front tracking applied to Rayleigh–Taylor instability," *SIAM (Soc. Ind. Appl. Math.) J. Sci. Comput.* **7**, 230 (1986).
- <sup>8</sup>G. Tryggvason, "Numerical simulations of the Rayleigh–Taylor instability," *J. Comput. Phys.* **75**, 253 (1988).
- <sup>9</sup>X. L. Li, "Study of three-dimensional Rayleigh–Taylor instability in compressible fluids through level set method and parallel computation," *Phys. Fluids A* **5**, 1904 (1993).
- <sup>10</sup>D. L. Youngs, "Numerical simulation of turbulent mixing by Rayleigh–Taylor instability," *Physica D* **12**, 32 (1984).
- <sup>11</sup>D. L. Youngs, "Modelling turbulent mixing by Rayleigh–Taylor instability," *Physica D* **37**, 270 (1989).
- <sup>12</sup>G. Tryggvason and S. O. Unverdi, "Computations of three-dimensional Rayleigh–Taylor instability," *Phys. Fluids A* **2**, 656 (1990).
- <sup>13</sup>T. Yabe, H. Hoshino, and T. Tsuchiya, "Two- and three-dimensional behavior of Rayleigh–Taylor and Kelvin–Helmholtz instabilities," *Phys. Rev. A* **44**, 2756 (1991).
- <sup>14</sup>X. L. Li, B. X. Jin, and J. Glimm, "Numerical study for the three-dimensional Rayleigh–Taylor instability through the TVD/AC scheme and parallel computation," *J. Comput. Phys.* **126**, 343 (1996).
- <sup>15</sup>J. Glimm, J. W. Grove, X. L. Li et al., "3-dimensional front tracking," *SIAM (Soc. Ind. Appl. Math.) J. Sci. Comput.* **19**, 703 (1998).
- <sup>16</sup>J. Glimm, J. Grove, X. L. Li, and D. C. Tan, "Robust computational algorithm for dynamic interface tracking in three dimensions," <http://www.ams.sunysb.edu/papers/papers98.html> (1998).
- <sup>17</sup>S. Chen and G. D. Doolen, "Lattice Boltzmann method for fluid flows," *Annu. Rev. Fluid Mech.* **30**, 329 (1998).
- <sup>18</sup>A. K. Gunstensen, D. H. Rothman, S. Zaleski, and G. Zanetti, "Lattice Boltzmann model of immiscible fluids," *Phys. Rev. A* **43**, 4320 (1991).
- <sup>19</sup>X. Shan and H. Chen, "Lattice Boltzmann model for simulating flows with multiple phases and components," *Phys. Rev. E* **47**, 1815 (1993).
- <sup>20</sup>M. R. Swift, W. R. Osborn, and J. M. Yeomans, "Lattice Boltzmann simulation of nonideal fluids," *Phys. Rev. Lett.* **75**, 830 (1995).
- <sup>21</sup>X. He, X. Shan, and G. D. Doolen, "A discrete Boltzmann equation model for non-ideal gases," *Phys. Rev. E* **57**, R13 (1998).
- <sup>22</sup>X. He, S. Chen, and R. Zhang, "A lattice Boltzmann scheme for incompressible multiphase flow and its application in simulation of Rayleigh–Taylor instability," *J. Comput. Phys.* (in press).
- <sup>23</sup>P. L. Bhatnagar, E. P. Gross, and M. Krook, "A model for collision process in gases. I: small amplitude processes in charged and neutral one-component system," *Phys. Rev.* **94**, 511 (1954).
- <sup>24</sup>U. Frisch, B. Hasslacher, and Y. Pomeau, "Lattice-gas automata for the Navier–Stokes equations," *Phys. Rev. Lett.* **56**, 1505 (1986).
- <sup>25</sup>X. He and L. Luo, "A priori derivation of the lattice Boltzmann equation," *Phys. Rev. E* **55**, R6333 (1997).
- <sup>26</sup>S. Chen, Z. Wang, X. Shan, and G. D. Doolen, "Lattice Boltzmann computational fluid dynamics in three dimensions," *J. Stat. Phys.* **68**, 379 (1992).
- <sup>27</sup>R. Evans, "The nature of the liquid–vapor interface and other topics in the statistical mechanics of nonuniform, classical fluids," *Adv. Phys.* **28**, 143 (1979).
- <sup>28</sup>B. T. Nadiga and S. Zaleski, "Investigations of a two-phase fluid model," *Eur. J. Mech. B/Fluids* **15**, 885 (1996).
- <sup>29</sup>J. S. Rowlinson and B. Widom, *Molecular Theory of Capillarity* (Oxford University Press, New York, 1982).
- <sup>30</sup>S. Chapman and T. G. Cowling, *The Mathematical Theory of Nonuniform Gases*, 3rd ed. (Cambridge University Press, Cambridge, 1970).
- <sup>31</sup>N. F. Carnahan and K. E. Starling, "Equation of state for nonattracting rigid spheres," *J. Chem. Phys.* **51**, 635 (1969).
- <sup>32</sup>S. I. Abarzhi, "Stable steady flow in the Rayleigh–Taylor instability," *Phys. Rev. Lett.* **81**, 337 (1998).
- <sup>33</sup>Q. Zhang and M. J. Graham, "A numerical study of Richtmyer–Meshkov instability driven by cylindrical shocks," *Phys. Fluids* **10**, 974 (1998).
- <sup>34</sup>D. L. Youngs, "Three-dimensional numerical simulation of turbulent mixing by Rayleigh–Taylor instability," *Phys. Fluids A* **3**, 1312 (1991).